# Electron-Impact Excitation and Ionization in Air

Winifred M. Huo[1]

*Huo Consulting LLC, Los Altos, CA 94024-3168*

Electron-impact ionization of N and $N_2$ and radiative recombination of $N^+$ and $O^+$ with electrons are studied in order to provide state-of-the-art data for CFD and radiation simulations in an ionized hypersonic flow. The electron-impact ionization rate coefficients of N are determined assuming Boltzmann equilibrium among the three lowest states, $^4S^o$, $^2D^o$, and $^2P^o$. They are significantly smaller that the rate data employed in the Park model, but are in reasonable agreement with the Losev model. For $N_2$, the calculated rate coefficients are larger than the Losev model below 25,000 K. The study of the radiative recombination of $N^+$ and $O^+$ shows that more than 93% of the radiation from this process is emitted in the 50-120 nm range. Due to the continuous nature of the radiation from recombination, it contributes a significant portion of the radiative heat load in the VUV region.

# Nomenclature

| | | |
|---|---|---|
| $A$ | = | neutral atom or molecule |
| $A^+$ | = | ion |
| $c$ | = | speed of light |
| $e$ | = | electron |
| $E_{A+}$ | = | energy of ion in ($n\,'l\,'s\,'$) state |
| $E_e$ | = | free electron energy |
| $E_{IP}$ | = | ionization energy of atom in ($nls$) state |
| $F$ | = | cumulative fraction of integrated radiation intensity |
| $h$ | = | Planck's constant |
| $k_B$ | = | Boltzmann constant |
| $k_I$ | = | electron-impact ionization rate coefficient |
| $k_{n\,'l\,'s\,'-nls}$ | = | radiative recombination rate coefficient of ion in ($n\,'l\,'s\,'$) state to neutral in ($nls$) state |
| $l$ | = | angular momentum quantum number of neutral atom |
| $l\,'$ | = | angular momentum quantum number of ion |
| $n$ | = | principal quantum number of neutral atom |
| $n\,'$ | = | principal quantum number of ion |
| $N_e$ | = | electron number density |
| $N_{ion}$ | = | ion number density |
| $N_{N+}$ | = | nitrogen ion number density |
| $N_{O+}$ | = | oxygen ion number density |
| $R$ | = | radiance |
| $R_{total}$ | = | total radiance |
| RR | = | radiative recombination |
| $s$ | = | spin quantum number of neutral atom |
| $s\,'$ | = | spin quantum number of ion |
| $t$ | = | time |
| $T_e$ | = | electron temperature |

[1] Principal Scientist, Huo Consulting LLC, 680 Blinn Court, Member AIAA.

| $\bar{v}_e$ | = | average electron velocity |
|---|---|---|
| $\varepsilon$ | = | scaled electron energy |
| $\lambda$ | = | photon wavelength |
| $\nu$ | = | photon frequency |
| $\sigma_I$ | = | electron-impact ionization cross-section |
| $\sigma_{BinaryEncounter}$ | = | Binary-Encounter cross-section |
| $\sigma_{DipoleBorn}$ | = | Dipole Born cross-section |
| $\sigma_{n'l's' \to nls}$ | = | radiative recombination cross-section of ion in ($n'l's'$) state to neutral in ($nls$) state |
| $<\sigma_{n'l's' \to nls}>$ | = | average radiative recombination cross-section of ion in ($n'l's'$) state to neutral in ($nls$) state |

## I. Introduction

During the hypersonic entry of a space vehicle into a planetary atmosphere, the flow field is ionized. The percentage of ionization depends on the entry speed and the vehicle size. In this regime, electron collision provides an efficient means of producing electronic excited states of atoms and molecules. The latter in turn are the source of radiation observed during a hypersonic entry. The rate coefficients for the production of electrons are part of the chemical reaction data set for Earth entry models and have been included in the data sets developed by Park[1,2], Losev[3] and Bird's TCE[4,5] models. Furthermore, in the non-equilibrium regime where the populations of radiative species are determined by the quasi-steady-state approximation, the electron number density, temperature, and excitation rate coefficients are part of the input data for QSS calculations. Another process that depends on electron number density and temperature is the radiative recombination of positive ions with electrons. As part of a systematic development of physics-based models of non-equilibrium chemistry and radiation in a hypersonic flow, it is timely to investigate and update the electron collision cross-sections/rate coefficients used in such models.

Associative ionization and electron-impact ionization are two production mechanisms of electrons in a hypersonic flow field. The rate data have been included in various chemistry models for Earth entry. Current rate data generally are based on dated experiments. For example, in the Park model the electron-impact ionization data are based on older shock tube experiments[6] with multiple processes occurring simultaneously. Modern day beam experiments, on the other hand, are performed under better-controlled conditions and with significant better energy resolution. However, beam measurements use target atoms or molecules at a specific energy level (mostly ground level) whereas a chemistry model for hypersonic simulations requires data for atoms/molecules with an energy distribution. Thus there is a gap in the beam data. For the purpose of developing electron impact data, present day quantum mechanical calculation is efficient and has a track record of reliability. It offers an alternate data source. In this paper quantum mechanical calculations are used to determine the rate coefficients for electron production in air.

Radiative recombination (RR) is a free-bound transition where the emitted photons cover the full range of frequencies. Currently in the NEQAIR[8] code, the emissivity of RR is determined from the absorptivity of the reverse reaction, photoionization (PI), whereas the PI absorptiviity is obtained using hydrogenic cross-section modified by a Gaunt factor. Recent studies of RR have provided data surpassing what is used in NEQAIR. Badnell[9] reported final-state resolved RR rate coefficients from the initial ground and metastable levels of $N^+$ and $O^+$. The data are available on the AMDPP (Atomic and Molecular Diagnostic Processes in Plasmas) website.[10] Nahar and Pradhan[11] reported RR rate coefficients from the ground state of $N^+$ and Nahar[12] reported RR data for the ground state of $O^+$. Employing the new data to determine the radiative intensity from RR is another goal of the present study.

## II. Electron-impact Ionization of N and $N_2$

Quantum theory has a demonstrated record of successful calculations of the total ionization cross-sections by electron impact.[13]

$$A + e \to A^+ + 2e. \tag{1}$$

The Binary-Encounter-Dipole (BED) model of electron-impact ionization developed by Kim and Rudd[14] has been used for a large variety of atoms and molecules and the BED cross-sections are available in the NIST database.[15] The improved Binary-Encounter-Dipole (iBED) model[16] was introduced in 2001 to improve the treatment of the dipole term in the BED model. In the iBED model, the total ionization cross-section is given by

$$\sigma_I = \sigma_{BinaryEncounter} + \sigma_{BornDipole}. \tag{2}$$

The Binary-Encounter cross-section $\sigma_{BinaryEncounter}$ is the modified Mott cross-section with the incident electron energy replaced by the average energy from the Binary-Encounter model.[17] The Dipole Born cross-section $\sigma_{DipoleBorn}$ is expressed by a three-term polynomial expansion of the generalized oscillator strength. The difference between the iBED and BED models lies in the use of the Dipole Born cross-section instead of the Dipole Bethe cross-section. The former includes the effect of electron shielding, thus improving the description of the process at low incident electron energies.

### A. Electron-impact ionization of N

The three lowest N states are the ground electronic state ($^4S^o$) and two lowest metastable states ($^2D^o$ and $^2P^o$). The $^2D^o$ state lies at 19,224.5 cm$^{-1}$ and the $^2P^o$ state at 28,838.9 cm$^{-1}$ above the ground state. All three states have significant populations at temperatures relevant to hypersonic entry. We investigate the following three reactions.

$$N(^4S^o) + e \rightarrow N^+ + 2e, \tag{3a}$$

$$N(^2D^o) + e \rightarrow N^+ + 2e, \tag{3b}$$

$$N(^2P^o) + e \rightarrow N^+ + 2e. \tag{3c}$$
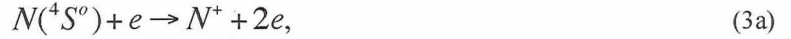
There are two ionization mechanisms. The first is direct ionization where the colliding electron directly detaches a bound electron from the atom or molecule. For the $^2D^o$ and $^2P^o$ states, a second mechanism named autoionization is also known to occur. Autoionization is an indirect process where the atom is first excited to a bound electronic state that lies in the continuum. The bound state is sufficiently energetic that it automatically ionizes.

$$N(^2D^o) + e \rightarrow N^* \rightarrow N^+ + 2e, \tag{3d}$$

$$N(^2P^o) + e \rightarrow N^* \rightarrow N^+ + 2e. \tag{3e}$$

For both $^2D^o$ and $^2P^o$ states, the autoionized state $N^*$ has been identified as the $2s^2 2p^2 ns$ $^2D$ state.
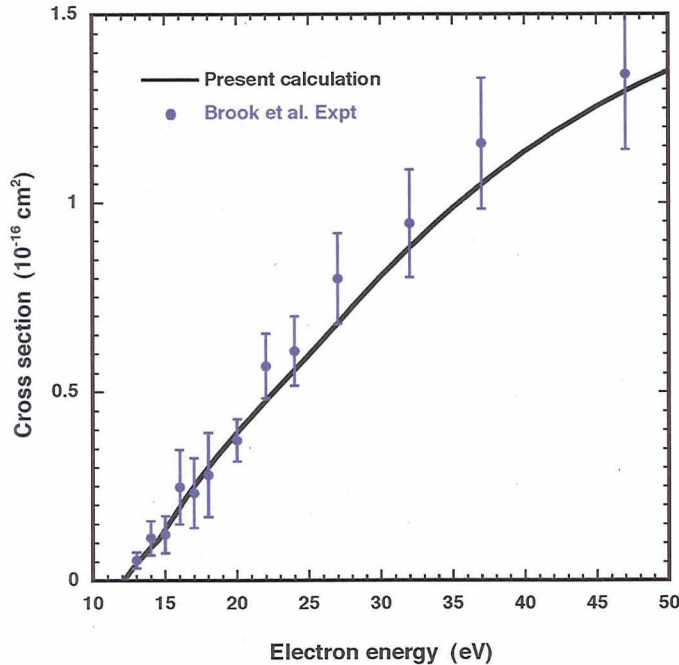
Figure 1. Ionization cross-section as a function of free electron energy for a mixture of N atoms composed of 70% $^4S^0$ and 30% $^2D^0$. Experimental data are from Brook et al.[19]

The iBED model is used to determine the direct ionization cross-sections. Excitation cross-sections to the autoionized state in (3d) and (3e) have been calculated by Kim and Desclaux[18] and their values are used here. The ionization cross-sections for $N(^2D^0)$ and $N(^2P^0)$ states are a sum of the direct and autoionization cross-sections.

A cross-beam measurement of the ionization cross-section for N atom has been reported by Brook et al.[19] The composition of the N atom beam used in the experiment has been analyzed by Kim and Desclaux[18] to be approximately 70% $^4S^0$ and 30% $^2D^0$. Figure 1 presents the calculated electron-impact ionization cross-section for such mixture of N atoms and compares with experiment. The reported experimental error is ± 40% at low energies and ± 15% at higher energies. As seen in the Figure, the calculated cross-sections agree with experiment to within their error estimate.
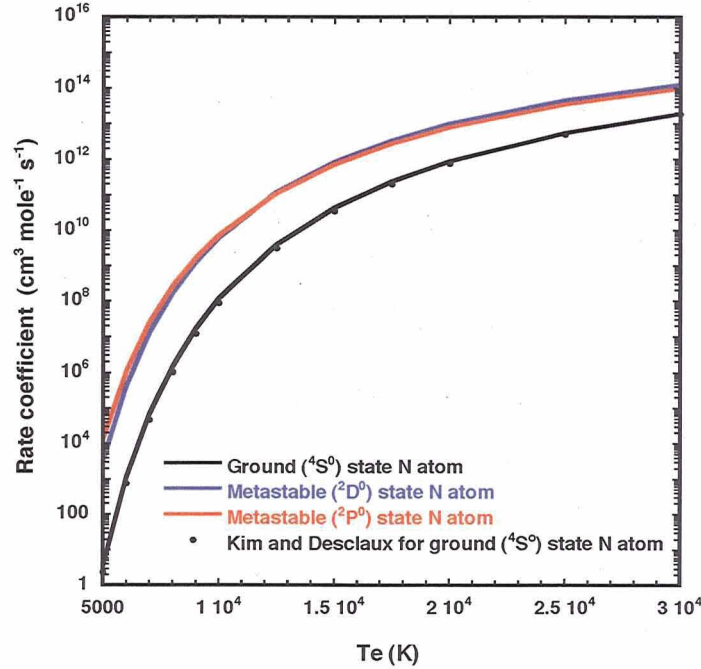


Figure 2. Electron-impact ionization rate coefficients of N atom in the ground ($^4S^0$) and two lowest metastable states ($^2D^0$ and $^2P^0$) as a function of free electron temperature. Also presented is the rate coefficient for the ground state calculated using the cross-section data of Kim and Desclaux.[18]

Figure 2 presents the ionization rate coefficients ($k_I$) as a function of electron temperature for N atom in the ground and two metastable states. The ionization threshold of the ground $^4S^0$ state is 117,225.4 cm^{-1}, for the metastable $^2D^0$ state it is 97,995.3 cm^{-1} and for the $^2P^0$ state it is 88,391.1 cm^{-1}. Due to the lower ionization thresholds for the metastable atoms, their $k_I$ are significantly larger than the ground state atom, particularly at low electron temperature. On the other hand, the $k_I$ for $^2D^0$ and $^2P^0$ states are close to each other even though the $^2P^0$ state has a lower ionization threshold. This is due to the larger autoionization contributions in the $^2D^0$ state. The $k_I$ for the ground state calculated using the data of Kim and Desclaux[18] is also presented in Figure 2 and it is in good agreement with the present calculation.

Figure 3 presents $k_I$ as a function of free electron temperature for three types of N atoms. In the first, the N atoms are in the ground state. In the second, the electronic temperature of the N atoms is assumed to be 10,000 K and an equilibrium distribution among the ground and the two metastable atoms is assumed. For the third type, the electronic temperature is 20,000 K and an equilibrium distribution is also assumed. The number density of the metastable atoms increases with electronic temperature. Because the $k_I$ for the metastable atoms is larger than that of

the ground state atoms, increasing the number density of the metastables at higher electronic temperatures increases the overall ionization rate coefficients. The $k_I$ for N atom from the Park93[1,2] and Losev94[3] models are also presented. In all cases, the calculated rate coefficients are more than one order of magnitude smaller than the data used in Park93 model. The rate data used in the Losev94 model, on the other hand, is reasonably close to our result. At $T_e$ lower than 10,000 K, Losev's rate coefficients are close to our rate coefficients for ground state N atoms. For $T_e$ above 10,000 K, his rate coefficients approaches our data determined assuming an N-atom electronic temperature at 10,000 K.
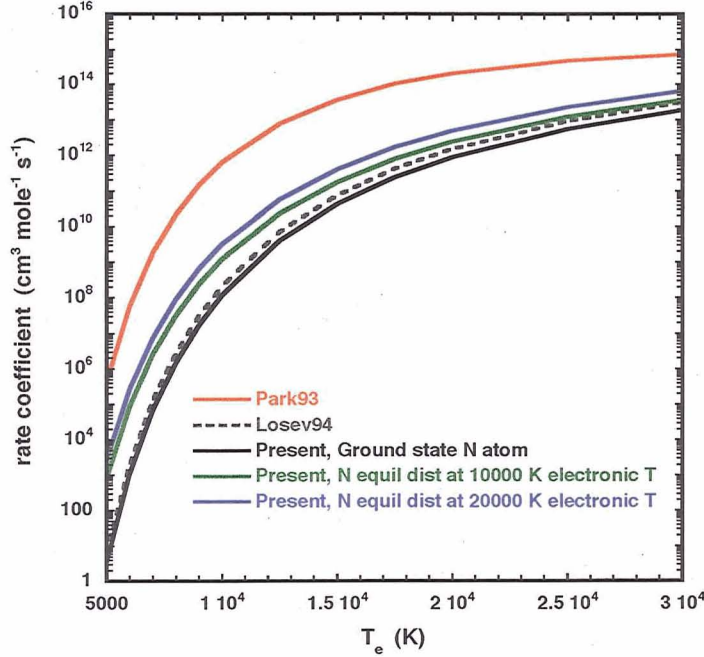


Figure 3. Electron-impact ionization rate coefficients of N atom as a function of free electron temperature. The rate coefficients from Park93[1,2] and Losev94[3] models are also presented.

## B. Electron-impact ionization of $N_2$

We use the iBED model to study electron-impact excitation of the ground ($X^1\Sigma_g^+$) state and the first excited state ($A^3\Sigma_u^+$) state of $N_2$.

$$N_2(X^1\Sigma_g^+) + e \rightarrow N_2^+ + 2e, \tag{4a}$$

$$N_2(A^3\Sigma_u^+) + e \rightarrow N_2^+ + 2e, \tag{4b}$$

The ionization potential of the $X^1\Sigma_g^+$ state is 125,660.1 cm$^{-1}$ at its equilibrium internuclear distance. Experimental measurements have shown no indication of significant autoionization effects in reaction (4a). Thus the present study treats only direct ionization. Figure 4 presents the calculated cross-section for reaction (4a) and comparison with two sets of experimental data, those by Straub at el.[19] and an older measurement by Rapp and Englander.[20] The estimated error in the data of Straub et al. is ±5% whereas for Rapp and Englander's data it is ±15%. The calculated cross-section is in excellent agreement with Rapp and Englander's data and is slightly larger than the data of Straub et al.

The ionization potential of the $A^3\Sigma_u^+$ state is 87,344.9 cm$^{-1}$ at its equilibrium internuclear distance. The adiabatic excitation energy from the ground state is 50,203.6 cm$^{-1}$. The present calculation is carried out at the experimental equilibrium internuclear distance of the $A$ state. Due to its lower ionization potential, the ionization rate coefficient of the $A$ state is larger than the ground state, especially at lower electron temperature. Figure 5 presents $k_I$ of $N_2$ as a function of free electron temperature for the ground state $N_2$, and equilibrium distributions of the $X$ and $A$ states at electronic temperature 10,000 K and 20,000 K, respectively. Due to its lower ionization

potential, the presence of the *A* state significantly increases the $k_I$ at low $T_e$. At higher $T_e$ its influence is less significant. The Park93 model does not include electron-impact ionization of $N_2$, but it is included in the Losev94 model. Below 25,000 K, $k_I$ from the Losev94 model is consistently smaller than all three sets of calculated data. At 25,000 K and above, the Losev94 data becomes larger than the theoretical values.
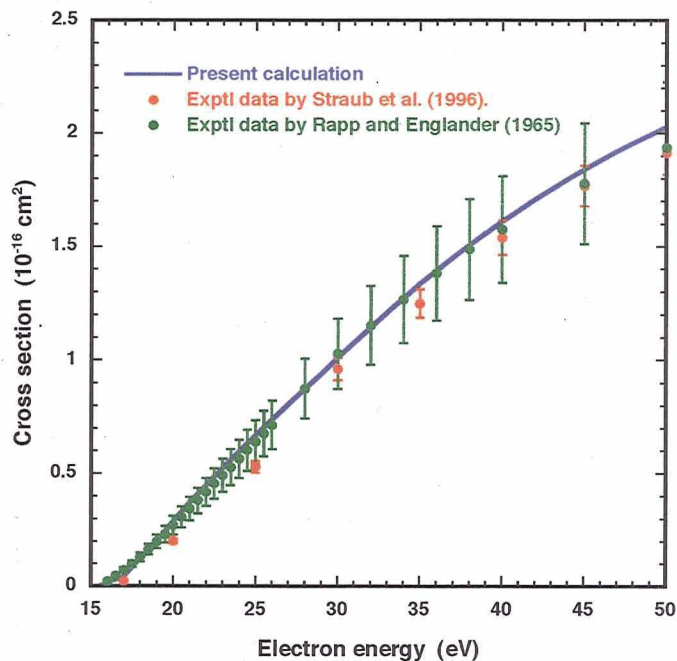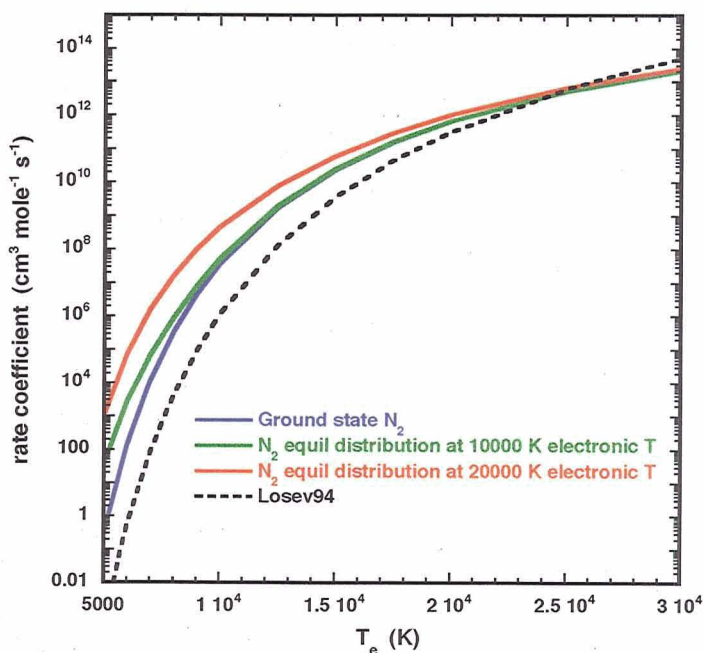


Figure 4. Ionization cross-section of $N_2$ molecule as a function of free electron energy. Experimental data from Straub et al.[19] and Rapp and Englander[20] are also presented.

Figure 5. Electron-impact ionization rate coefficients of $N_2$ molecule as a function of free electron temperature. The rate coefficients from Losev94[3] model are also presented

# III.  Radiative Recombination of $N^+$ and $O^+$

Radiative recombination of a positive ion with an electron

$$A^+(n'l's') + e \rightarrow A(nls) + h\nu \tag{5}$$

produces photon with energy $h\nu = E_{A+} + E_{IP} - E_e$. The radiative power produced by the RR of an ion in the $(n'l's')$ state to a neutral atom in the $(nls)$ state is given by[21]

$$\left\langle \frac{d(h\nu)}{dt} \right\rangle = N_e \overline{v}_e \int_0^\infty \varepsilon h\nu \sigma_{n'l's'-nls}(\varepsilon) \exp(-\varepsilon) d\varepsilon. \tag{6}$$

Here $\varepsilon = E_e/k_B T_e$ is the electron energy scaled by $k_B T_e$. In terms of the photon wavelength Eq. (6) is rewritten as

$$\left\langle \frac{d(h\nu)}{dt} \right\rangle = N_e \overline{v}_e \frac{hc}{k_B T_e} \int_0^\infty \varepsilon h\nu \sigma_{n'l's'-nls}(\varepsilon) \exp(-\varepsilon) \lambda^{-2} d\lambda. \tag{7}$$

Thus the radiance $R$ produced at wavelength $\lambda$ by the RR of $A^+$ ions in the $(n'l's')$ state to all neutral states is

$$R(\lambda) = (4\pi\lambda^3 k_B T_e)^{-1} h^2 c^2 N_{ion} N_e \overline{v}_e \sum_{nls} \varepsilon \sigma_{n'l's'-nls}(\varepsilon) \exp(-\varepsilon). \tag{8}$$

The total radiance $R_{total}$ is obtained by integrating over the photon wavelength

$$R_{total} = \int_0^\infty R(\lambda) d\lambda. \tag{9}$$

The RR rate coefficients tabulated in the literature[10,11,12] is related to the RR cross-section by

$$k_{n'l's-nls}(T_e) = \overline{v}_e \int_0^\infty \varepsilon \sigma_{n'l's'-nls}(\varepsilon) \exp(-\varepsilon) d\varepsilon. \tag{10}$$

To determine $\sigma_{n'l's'-nls}$ by inverting the rate coefficient data tend to produce unphysical results. Instead the average cross-section[21] is used.

$$\sigma_{n'l's'-nls}(E_e) \approx \left\langle \sigma_{n'l's'-nls}(T_e) \right\rangle = \int_0^\infty \varepsilon \sigma_{n'l's'-nls}(\varepsilon) \exp(-\varepsilon) d\varepsilon = \frac{k_{n'l's'-nls}(T_e)}{\overline{v}_e}. \tag{11}$$

## A.  Radiative recombination of $N^+$

The AMDPP website[10] provides RR rate coefficients of $N^+$ to neutral N states up to $n = 8$ and $l = 7$. Under the *ls* coupling scheme, the calculation covers 4 ion states and 406 neutral states. Under *jj* coupling, there are 6 ion states and 1052 neutral states. In comparison, NIST database[22] lists 381 neutral N states under *jj* coupling. Temperature covered ranges from $10 - 10,000,000$ K. Nahar and Pradhan[11] also reported RR data of $N^+$. They cover

recombination to 20 neutral states, with highest $n = 4$, $l = 3$. Temperature range is $100 - 10,000$ K. Only one ion state is covered. Figure 6 compares the RR rate coefficients from AMDPP and from Nahar and Pradhan. For recombination from the ground ($^3P^o$) state of $N^+$ to the three lowest levels of N, $^4S^o$, $^2D^o$, and $^2P^o$, the two sets of data are consistent with each other, but significant deviations are found for recombination to a higher–lying state, $2s^22p^2(^3P^c)3p$ $^4P^o$, especially at low temperatures. However, it will be shown later in the section that radiative heat flux from RR is dominated by the transitions to the lowest-lying neutral states. Thus the deviation in the rate coefficients to higher-lying neutral states may have little effects in the heat flux calculation.
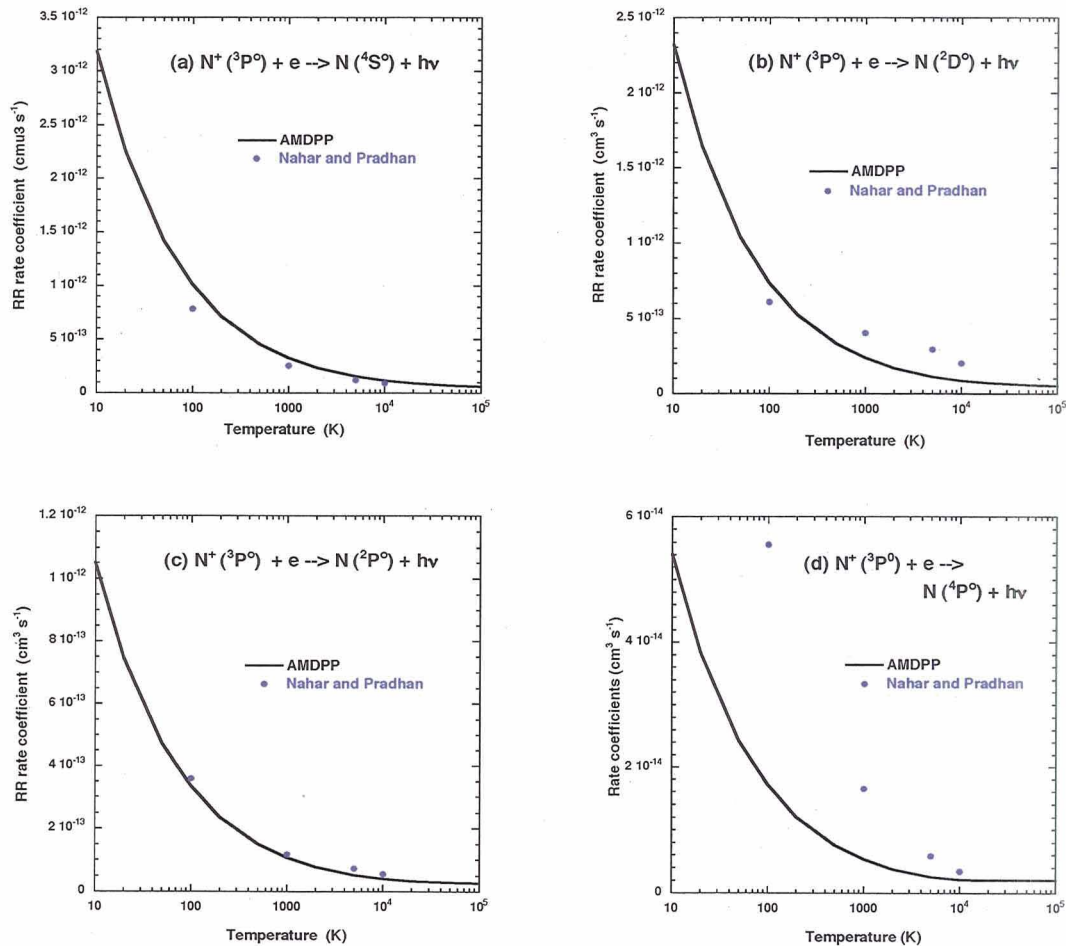


Figure 6. Comparison of state-to-state RR rate coefficients from the ground ($^3P^o$) state of $N^+$ to the three lowest states of N, $^4S^o$, $^2D^o$, $^2P^o$ and the $2s^22p^2(^3P^c)3p$ $^4P^o$ state of N. Solid line, data from AMDPP[10] and • data from Nahar and Pradhan.[11]

In the present calculation, we choose to use the AMDPP database because it covers four ion states in *ls* coupling. Two modifications were made to the AMDPP database. First, the energy levels of N and $N^+$ in the AMDPP database were determined using approximate quantum mechanical calculations. For most states, there are significant differences between the AMDPP values versus the NIST data. Hence all energy levels in the AMDPP database are replaced by the NIST data when possible. Scaling is used when the corresponding data are not available. For example, NIST lists energy levels of $2s^22p^2(^3P)8s$ $^2P$ and $2s^22p^2(^3P)8d$ $^4F$, $^2P$, $^2F$, $^2D$, $^4P$, and $^4D$, but does not list the energy levels generated from the 8p, 8f, 8g, 8h, 8i, and 8j electrons with the same ion core. The energies of those states are determined by scaling the AMDPP value with the difference between the AMDPP and NIST energies for the $2s^22p^2(^3P)8d$ levels. The second modification is to extend the number of neutral states that are formed by the recombination of the ground ($^3P^o$) state of $N^+$. By including all states up to $n=8$, $l=7$, AMDPP uses 179 neutral states

13

and the highest neutral state is 1593 cm$^{-1}$ from the dissociation limit. Since NIST lists energy levels up to $n$=12, i.e., $2s^22p^2(^3P)12d$, we generate additional 176 N levels from $n$=9 to 12 and $l$=0 to 7. For high $n$ states the RR rate coefficient is expected to vary slowly with $n$. Thus the RR rate coefficients for the additional states are assumed to be the same as $n$=8 levels. Table 1 lists the number of N states used in the recombination calculations of the four N$^+$ states. It is seen that the energy of the highest N state is 600.4 – 1,740.0 cm$^{-1}$ below the corresponding ionization limit. The lack of data on the high-lying N states increases the uncertainty in the RR radiance at the infrared spectrum, but not the UV spectrum.

Table 1. Number of states used in the RR calculations of N$^+$

| N$^+$ state | Number of N states | Energy of highest N state |
|---|---|---|
| $2s^22p^2\,^3P^o$ | 179 states from AMDPP | |
| | 176 states from extension | 600.4 cm$^{-1}$ below the ionization limit |
| $2s^22p^2\,^1D^o$ | 158 states from AMDPP | 1,235.2 cm$^{-1}$ below the ionization limit |
| $2s^22p^2\,^1S^o$ | 63 states from AMDPP | 625.8 cm$^{-1}$ below the ionization limit |
| $2s2p^3\,^5S^o$ | 68 states from AMDPP | 1,740.0 cm$^{-1}$ below the ionization limit |

The present calculation uses the parameters $T_e$ = 10,460 K, $N_e$ = 1.19×10$^{16}$ cm$^{-3}$, and $N_{N+}$ = 1.02×10$^{16}$ cm$^{-3}$. The calculation covers wavelengths from 10 nm to 10,000 nm. The radiance from the four N$^+$ states are weighed by the Boltzmann factor and summed. The electronic temperature of N$^+$ is assumed to be the same as the free electron temperature. The calculated radiance spectrum can be divided into three regions: (1) 120 – 10,000 nm, (2) 50 – 120 nm, and (3) 10 – 50 nm. In the first region, 120 nm - 10,000 nm, the RR spectrum is low-intensity, continuous and rather structureless, a typical background spectrum. Figure 7 shows part of the spectrum, from 150 – 1000 nm.
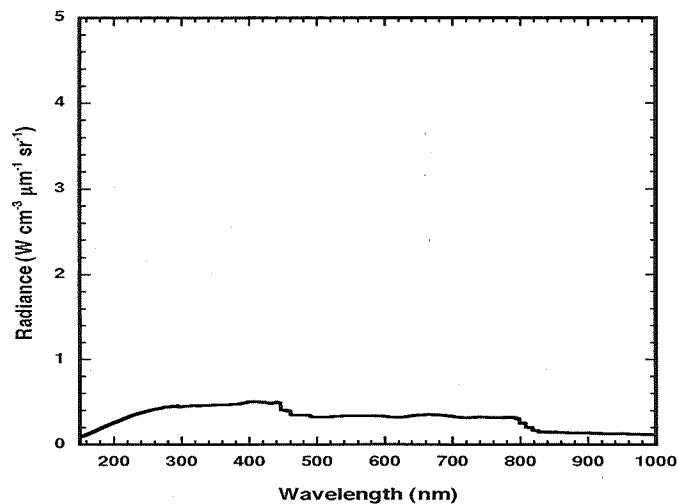


Figure 7. Radiance spectrum from RR of N$^+$, 150 – 1,000 nm.

The second region is 50 – 120 nm. Here the radiance spectrum, shown in Figure 8, is significantly more intense. It consists of a series of very sharp peaks, with a sharp, precipitous rise on the long wavelength side and a slower decrease on the short wavelength side. The onset of the sharp peaks are at 113.09, 101.97, 88.15, 85.25 nm. The maximum radiance in this region, at 85.25 nm, is 512.6 W cm$^{-3}$ µm$^{-1}$ sr$^{-1}$. By comparison, the maximum radiance in the 120-1000 nm region is 0.5 W cm$^{-3}$ µm$^{-1}$ sr$^{-1}$, which is approximately three orders of magnitude smaller. The large radiance and the continuous nature of the spectrum make this an important contribution to the radiative heat flux. To better understand the peak structure, Figure 9 shows the individual contribution from the four ion states, without the Boltzmann weight factor. The RR of the ground state ion shows three peaks, from recombination to the lowest three neutral states, $2s^22p^3\,^4S^o$, $^2D^o$, and $^2P^o$. The RR of the $^1D^o$ ion has two peaks, from recombination to the $2s^22p^3\,^2D^o$ and $^2P^o$ states of N. The RR of the $^1S^o$ ion has one peak for recombination to the $2s^22p^3\,^2P^o$ state of N. The

RR of the $^5S^o$ ion has two peaks from recombination to the $2s^2 2p^3$ $^4S^o$ and $2s2p^4$ $^4P$ of N. The sharp onset of each peak is a reflection of the characteristics of the RR process. As seen in Figure 6, the maximum of RR occurs at threshold electron energy, after which the rate goes down with electron energy. This is reflected in the decrease of radiance at the short wavelength side of the peak.
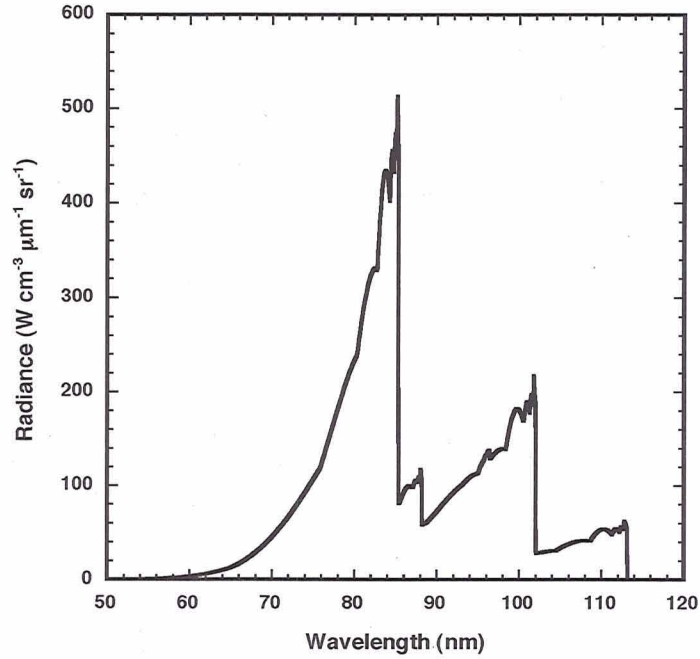


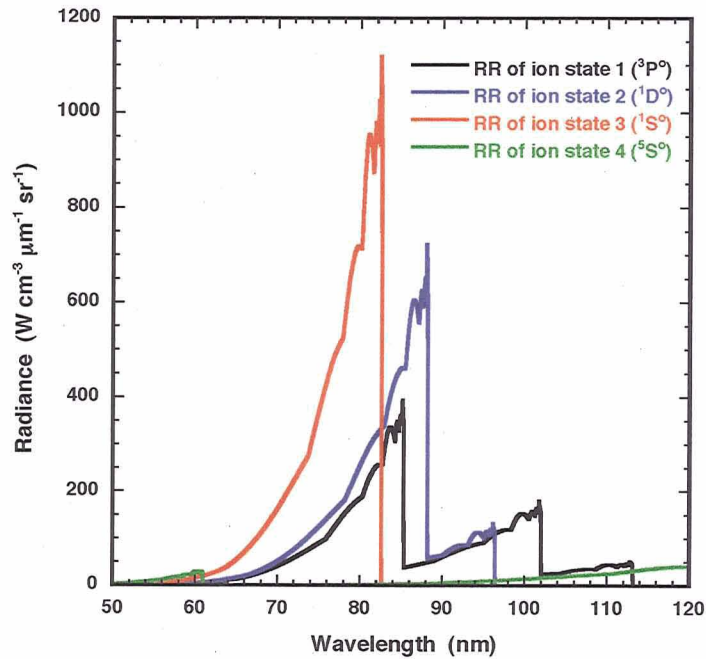Figure 8. Radiance spectrum from RR of $N^+$ in the 50 – 120 nm region.

Figure 9. Radiance spectrum from the RR of four lowest $N^+$ states.

In the third region, 10 - 50 nm, the radiance is extremely weak. Increasing the number of ion state used in the calculation may improve the spectrum. However, the higher-lying ion state has a small Boltzmann weight factor. Therefore they will not change the results in a meaningful way.

The total radiance $R_{total}$ from RR of $N^+$, from 10 – 10,000 nm is 6.11 W cm$^{-3}$ sr$^{-1}$. Total radiance from 120 – 10,000 nm is 0.35 W cm$^{-3}$ sr$^{-1}$.

## B. Radiative recombination of $O^+$

The AMDPP database[10] provides RR rate coefficients of $O^+$ to neutral O states up to $n = 8$ and $l = 7$. Under the $ls$ coupling scheme, the database covers 3 ion states and 623 O states. Under $jj$ coupling, there are 5 ion states and 1061 neutral states. In comparison, NIST database[22] lists 501 neutral O states under $jj$ coupling. Temperature covered by AMDPP ranges from 10 – 10,000,000 K. Nahar[12] reported RR data of $O^+$ covering recombination to 10 neutral states from the ground state ion. Highest $n = 6$, $l = 3$. Temperature range is 100 – 10,000 K. Figure 10 compares the RR rate coefficients from AMDPP and Nahar for the recombination of the ground ($^4S^o$) state of $O^+$ to the ground $^3P$ state and the $2s^2 2p^3(^4S^o)3d\ ^5D^o$ of O. (The recombination from the $^4S^o$ state of $O^+$ does not reach the metastable $^1D$, and $^1S$ states of O). The two sets of data agree with each other.
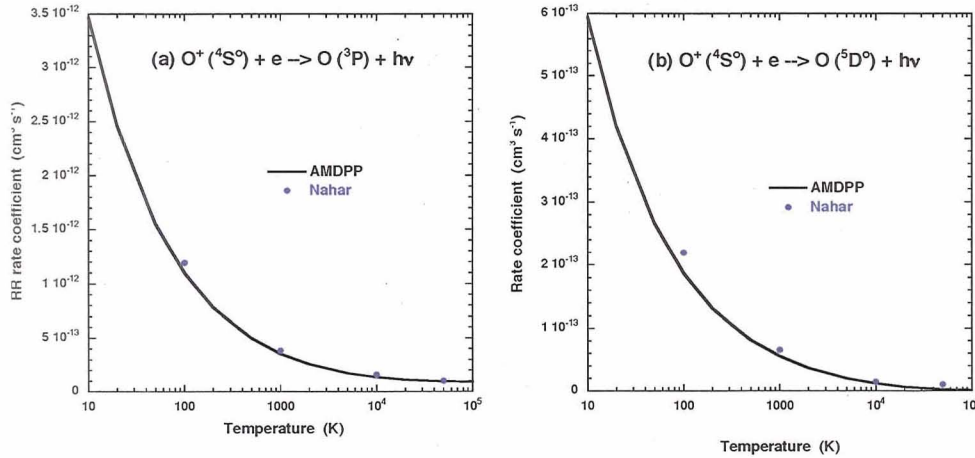


Figure 10. Comparison of state-to-state RR rate coefficients from the ground ($^4S^o$) state of $O^+$ to the ground $^3P$ and the $2s^2 2p^3(^4S^o)3d\ ^5D^o$ of O. Solid line, data from AMDPP[10] and • data from Nahar.[12]

As in the $N^+$ case, we choose to use the AMDPP database for our calculation. The AMDPP energy levels of the ion and neutral states are replaced either by the NIST data or by scaled values, using the same procedure as done for N. In addition, we make use of availability of NIST data for higher $n$ levels ($n = 31$ for states converging to the $^4S^o$ state of $O^+$. For states converging to the $^2D^o$ state of $O^+$, maximum $n = 16$) and generate additional N states. For states converging to the $^4S^o$ of $O^+$, 368 states from $n = 9 – 31$ and $l = 0 – 7$ are added. For states converging to the $^2D^o$ $O^+$ limit, 136 states from $n = 9 – 10$ and $l = 0 – 7$ are added. Table 2 lists the O states used in the RR calculation of the three $O^+$ ion states.

Table 2. Number of O states used in the RR calculations of $O^+$

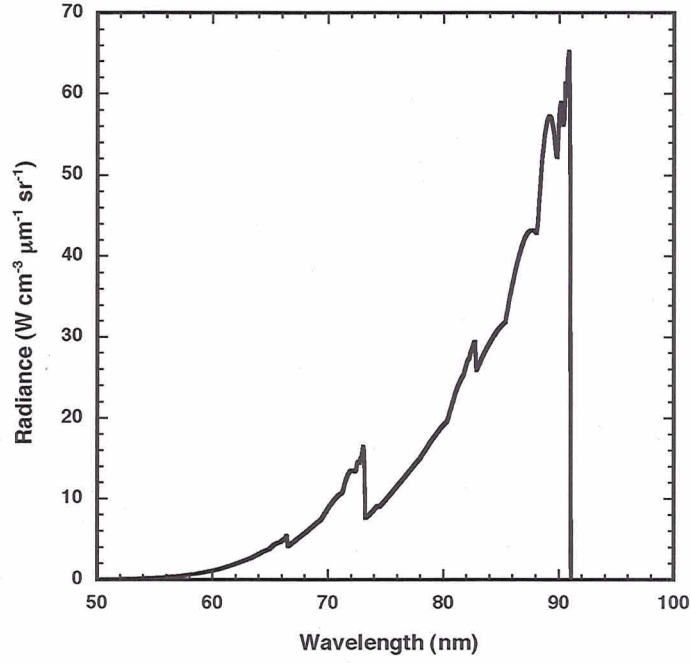| $O^+$ state | Number of O states | Energy of highest O state |
|---|---|---|
| $2s^2 2p^3\ ^4S^o$ | 67 states from AMDPP | |
| | 368 states from extension | 1,224.2 cm$^{-1}$ below the ionization limit |
| $2s^2 2p^3\ ^2D^o$ | 281 states from AMDPP | |
| | 136 states from extension | 1,078.8 cm$^{-1}$ below the ionization limit |
| $2s^2 2p^3\ ^2P^o$ | 275 states from AMDPP | 1,722.3 cm$^{-1}$ below the ionization limit |

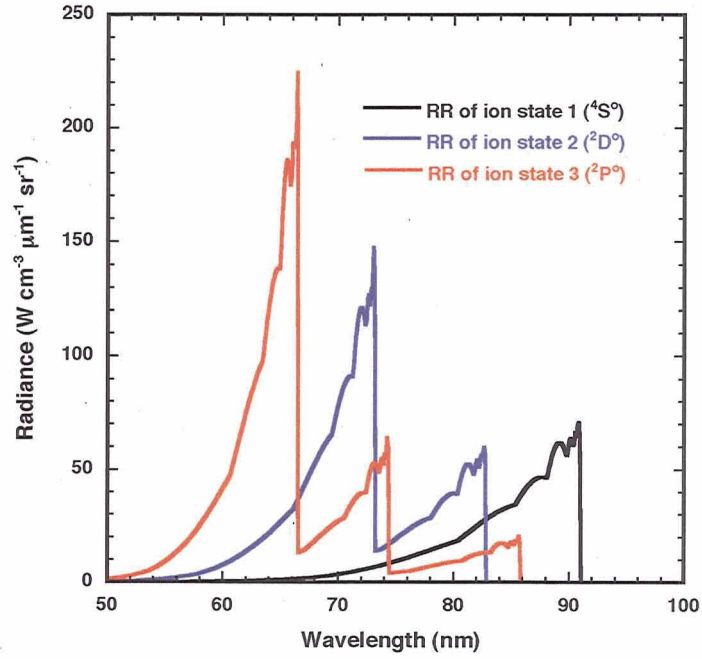Figure 11. Radiance spectrum from RR of $O^+$ in the 50 – 100 nm region



Figure 12. Radiance spectrum from the RR of three lowest $O^+$ states

The present calculation uses the parameters $T_e$ = 10,460 K, $N_e$ = 1.19×10$^{16}$ cm$^{-3}$, and $N_{O+}$ = 1.76×10$^{15}$ cm$^{-3}$ and covers wavelengths from 10 nm to 10,000 nm. As in the case of $N^+$ study, the radiance from the three $O^+$ states is

weighed by the Boltzmann factor and summed. The calculated radiance spectrum again can be divided into three regions: (1) 100 – 10,000 nm, (2) 50 – 100 nm, and (3) 10 – 50 nm. In the first region, the RR spectrum is weak and continuous, a typical background spectrum. The second region is significantly more intense, consisting of one strong peak and followed by a series of small peaks. The radiance spectrum at 50 – 100 nm is shown in Figure 11, and the contributions from the individual ion states, without the Boltzmann factor, are shown in Figure 12. The RR of the ground $^4S^o$ state of $O^+$ shows one peak, from the recombination to the ground $^3P$ state of O. The RR of the $^2D^o$ state of $O^+$ has two peaks, from combination to the ground $^3P$ and the $2s^22p^4\ ^1D$ states of O. The RR of the $^2P^o$ state of $O^+$ also has two peaks, from combination to the ground $^3P$ and the $2s^22p^4\ ^1D$ and $^1S$ states of O. In the third region the radiance spectrum again becomes very low in intensity.

The total radiance $R_{total}$ from RR of $O^+$, from 10 – 10,000 nm is 0.67 W cm$^{-3}$ sr$^{-1}$. Total radiance from 100 – 10,000 nm is 0.09 W cm$^{-3}$ sr$^{-1}$. The total radiance of $O^+$, from 10 – 10,000 nm is ~11% of the value for $N^+$.

## C. Comparison with NEQAIR result

The strong continuum emission from RR in the VUV region should contribute significantly to the radiative heat load. A comparison with NEQAIR simulation shows the role of RR in this model. Figure 13 presents a high-resolution spectrum of radiation during the entry of a large blunt body, provided by Dr. Dinesh Prabhu using NEQAIR. Below 120 nm, in addition to the series of sharp lines from bound-bound transitions there are four structures with a sharp onset and slower decrease at the short wavelength side, the same characteristics as the RR spectrum shown in Figures 8 and 11. These structures are distinctly different form the bound-bound transitions in the spectrum. The location of the four sharp onsets are in good agreement with onsets observed at 113.09, 101.97, and 85.25.nm in the $N^+$ RR spectrum and the 90.98 nm onset in the $O^+$ RR spectrum. Thus the NEQAIR calculation includes the major features in our RR spectrum, even though not all peak structures in our calculations are there.
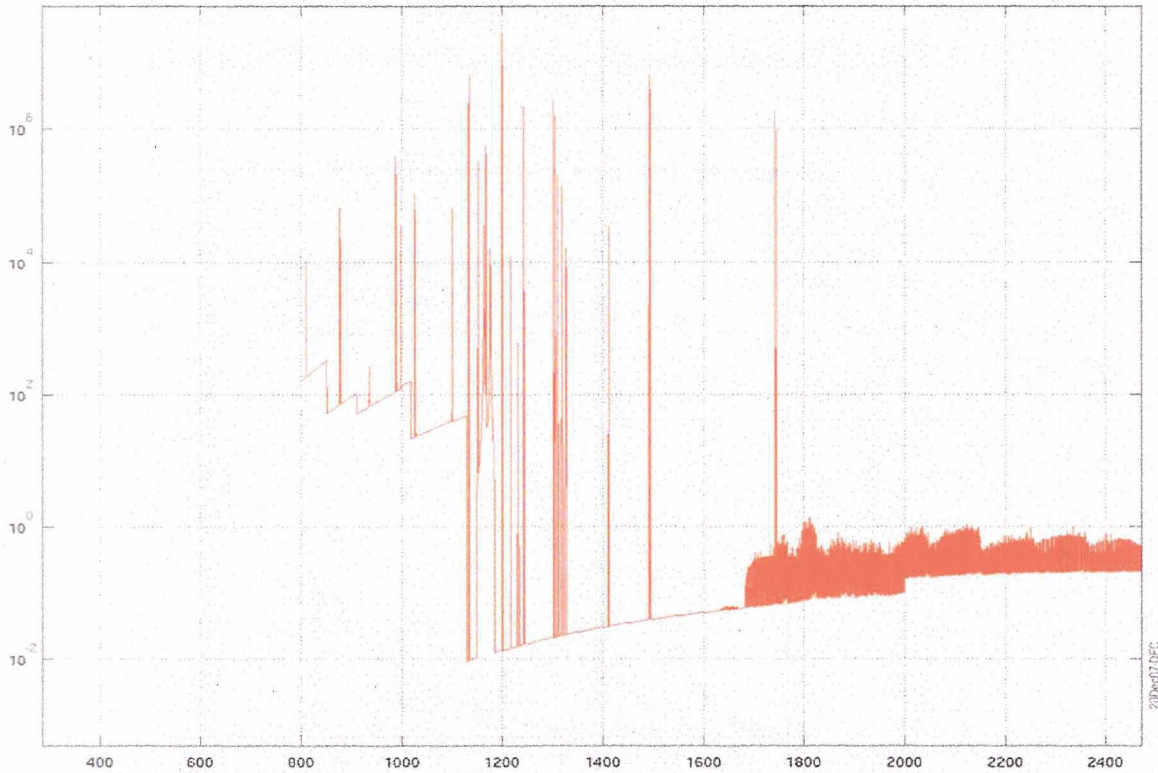


Figure 13. High-resolution spectrum from NEQAIR simulation (provided by Dr. Dinesh Prabhu). The y-axis is radiance (W cm$^{-3}$ $\mu$m$^{-1}$ sr$^{-1}$) and the x-axis is wavelength in Ångstrom.

Figure 14 presents the cumulative fraction of integrated radiation intensity, $F$, as a function of wavelength from Dr. Prabhu's NEQAIR calculation. For wavelengths longer than 115 nm, $F$ increases like a step function, a reflection that the contributions are from bound-bound transitions. However, between 90 nm to 115 nm, $F$ does not

behave like a step function. Instead, it smoothly increases to around 25% of the total intensity. This behavior reflects the continuous nature of the RR contribution. While the intensity of the RR radiation at a given wavelength is far smaller than the strong bound-bound transitions, the broadness of the spectrum is the source of the large contribution to $F$ from the RR transitions. Note that Figure 14 does not extend to 85nm and below, thus missing the strongest peak structure in the RR spectrum of $N^+$ at 85.25 nm, evident both our calculation in Figure 9 and the NEQAIR spectrum in Figure 13. The oxygen peak at 90.98 nm seen in Figures 11 and 13 is also absent. Thus the RR contribution to $F$ will increase if these contributions are included.

Based on both the present calculations and the NEQAIR simulation, it is evident that RR in the $50 - 120$ nm region contributes a significant portion to the radiative heat load. It is advisable that future calculations of radiative heat load should extend the spectrum down to at least 60 nm.
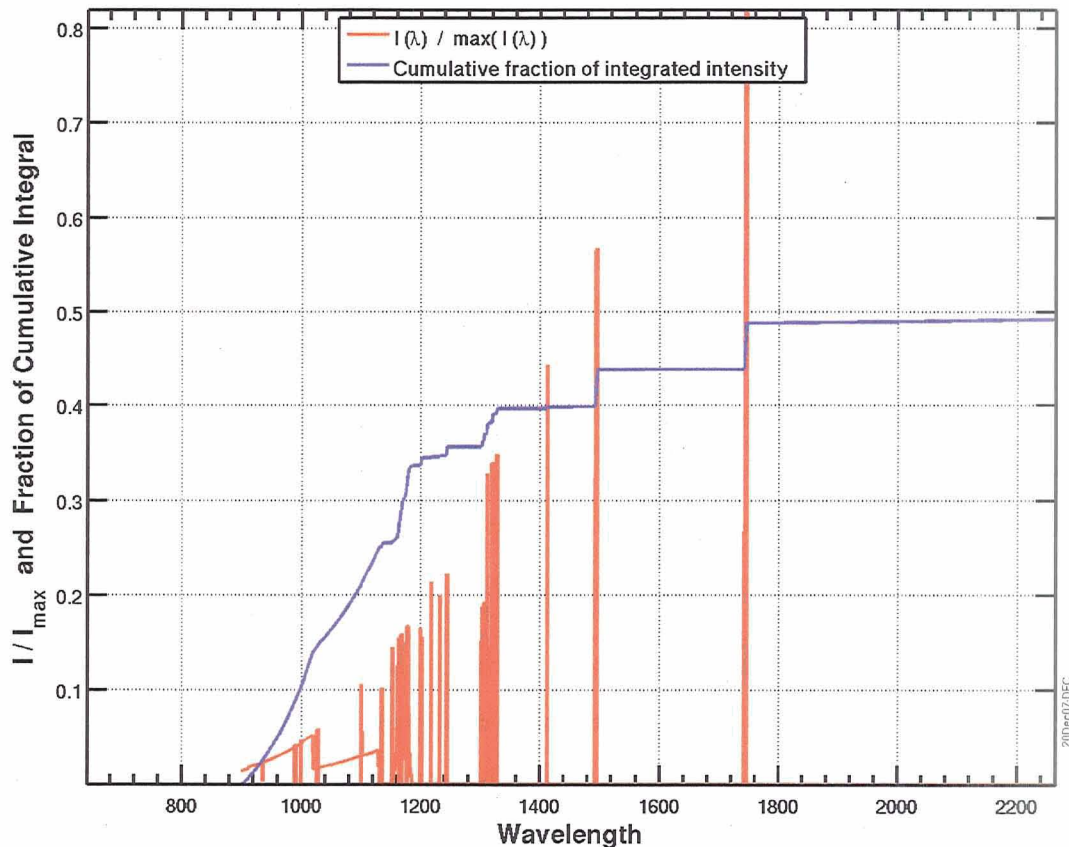


Figure 14. Cumulative fraction of integrated intensity as a function of photon wavelength. The wavelength is in Ångstrom

## IV.  Conclusion

This study finds significant differences between the new theoretical data of electron-impact ionization and those used in existing chemistry models. A change of the production rate of free electrons is likely to affect the time required for the free electron to reach equilibrium. Our study also shows that radiative recombination contributes a significant portion of the radiative heat load in the VUV region. Thus modeling of radiative heat load during high-speed entry to the Earth's atmosphere should cover radiation down to 60 nm. Experimental verification of the radiation from RR will be very valuable. Measurement of the first RR peak, at 113.09 nm, will serve to demonstrate the role of RR in radiative heating.

## Acknowledgments

## References

[1] Park, C., "Review of Chemical-Kinetic Problems of Future NASA Missions I. Earth Entries," *J. Thermophysics and Heat Transfer* Vol. 7 1993, pp. 385-398.

[2] Park, C., Jaffe, R. L., and Partridge, H., "Chemical-Kinetics Parameters of Hyperbolic Earth Entry," *J. Thermophysics and Heat Transfer* Vol. 15, 2001, pp.76-90.

[3] Losev, S. A., Makarov, V. N., Pogosbekyan, M. J., Shatalov, O .P., and Nikol'sky, V. S., "Thermo-chemical Nonequilibrium Kinetic Models in Strong Shock Waves of Air", AIAA Paper 94-1990, 1994.

[4] Bird, G. A., *Molecular Gas Dynamics and the Direct Simulations of Gas Flows*, Chap. 2, Clarendon, Oxford, England, U.K., 1994.

[5] Bird, G. A., "Monte-Carlo Simulation in an Engineering Context," *Rarefied Gas Dynamics*, edited by S. Fisher, Vol. 74, AIAA, New York, 1981, pp. 239-255.

[6] Park, C., *Nonequilibrium Hypersonic Aerothermodynamics*, John Wiley & Sons, New York, 1990.

[7] Park, C., "A Review of Reaction Rates in High Temperature Air", AIAA Paper 89-1740, 1989.

[8] Whiting, E. E., Park, C., Liu, Y., Arnold, J. O., and Patterson, J. A., "NEQAIR96, Nonequilibrium and Equilbrium Radiative Transport and Spectra Program: User's Manual", NASA Reference Publication 1389, 1996.

[9] Badnell, N. R., "Radiative recombination data for modeling dynamic finite-density plasmas," *The Astrophysical Journal Supplement Series* Vol. 167, 2006, pp. 334-342.

[10] URL:http://amdpp.phys.strath.ac.uk/tamoc/DATA/RR/.

[11] Nahar, S. N., and Pradhan, A. K., "Electron-ion recombination rate coefficients, photoionization cross sections, and ionization fractions for astrophysically abundant elements. I. Carbon and nitrogen," *The Astophysical Journal Supplement Series* Vol. 111, 1997, pp. 339-355.

[12] Nahar, S. N., "Electron-ion recombination rate coefficients, photoionization cross- ections, and ionization fractions for astrophysically abundant elements. II. Oxygen ions," *The Astophysical Journal Supplement Series* Vol. 120, 1999, pp. 131-145.

[13] Huo, W. M., and Kim, Y.-K., "Electron collision cross-section data for plasma modeling", *IEEE Transactions on Plasma Science*, Vol. 27, no. 5, 1999, pp. 1225-1240.

[14] Kim, Y.-K., and Rudd, M. E., "Binary-Encounter-Dipole Model for Electron-Impact ionization," *Physical Review A* Vol 50, 1994, pp. 3954-3967.

[15] URL: http://physics.nist.gov/PhysRefData/Ionization/index.html.

[16] Huo, W. M., "A convergent series representation of the generalized oscillator strength for electron-impact ionization and an improved Binary-Encounter Dipole model," *Physical Review* A, Vol. 64, 2001, pp. 042719-1 – 042719-16.

[17] Vriens, L., *Case Studies in Atomic Physics*, edited by E. W. McDaniel and M. R. C. McDowell, North-Holland, Amsterdam, 1969, Vol. 1, p. 335.

[18] Kim, Y.-K., and Desclaux, J. P., "Ionization of carbon, nitrogen, and oxygen by electron impact," *Physical Review A*, Vol. 66, 2002, pp. 012708-1 – 012708-12.

[19] Straub, H. C., Renault, P., Lindsay, B. G., Smith, K. A., and Stebbings, R. F., "Absolute partial cross sections for electron-impact ionization of $H_2$, $N_2$, and $O_2$ from threshold to 1000 eV," *Physical Review. A*, Vol. 54, 1996, pp. 2146-2153.

[20] Rapp, D., and Englander-Golden, P., "Total cross-sections for ionization and attachment in gases by electron impact. I. Positive ionization," *Joural of Chemical Physics*, Vol. 43, 1965, pp.1464-1479.

[21] Flannery, M. R., "Electron-Ion and Ion-Ion Recombination," *Atomic, Molecular, & Optical Physics Handbook*, edited by G. W. F. Drake, American Institute of Physics, Woodbury, New York, 1996 pp. 605-620.

[22] URL:http://physics.nist.gov/PhysRefData/contents.html.